HHS Public Access

Author manuscript

Gastroenterology. Author manuscript; available in PMC 2023 April 01.

Published in final edited form as:

Gastroenterology. 2022 April ; 162(4): 1303–1318.e18. doi:10.1053/j.gastro.2021.12.273.

Loss of *Rnf43* accelerates *Kras*-mediated neoplasia and remodels the tumor immune microenvironment in pancreatic adenocarcinoma

Abdel Nasser Hosein[1,2,3], **Gita Dangol**[1], **Takashi Okumura**[1], **Jason Roszik**[4], **Kimal Rajapakshe**[1], **Megan Siemann**[1], **Mohamed Zaid**[5], **Bidyut Ghosh**[1], **Maria Monberg**[1], **Paola A. Guerrero**[1], **Aatur Singhi**[7], **Cara L Haymaker**[1], **Hans Clevers**[6], **Lotfi Abou-Elkacem**[1], **Sonja M. Woermann**[1,*], **Anirban Maitra**[1,*]

[1.]Department of Translational Molecular Pathology, Ahmad Center for Pancreatic Cancer Research, The University of Texas MD Anderson Cancer Center, Houston, Texas, USA.

[2.]Department of Internal Medicine, Division of Hematology & Oncology, The University of Texas Southwestern Medical Center, Dallas, Texas, USA.

[3.]Advocate Aurora Health, Vince Lombardi Cancer Clinic - Sheboygan, Wisconsin, USA.

[4.]Department of Melanoma Medical Oncology Research, Division of Cancer Medicine, The University of Texas MD Anderson Cancer Center, Houston, Texas, USA.

[5.]Department of Radiation Oncology, The University of Texas MD Anderson Cancer Center, Houston, Texas, USA.

[6.]Oncode Institute, Hubrecht Institute, Royal Netherlands Academy of Arts and Sciences, University Medical Center Utrecht and Princess Maxima Center, Utrecht, the Netherlands.

[7.]Department of Pathology, University of Pittsburgh Medical Center, Pittsburgh, Pennsylvania, USA.

Abstract

[*]**Correspondence**: Anirban Maitra, MBBS, Department of Translational Molecular Pathology, Sheikh Ahmed Center for Pancreatic Cancer Research, The University of Texas MD Anderson Cancer Center, Houston, Texas 77030, USA. amaitra@mdanderson.org.

Author Contributions:

ANH: conceptualized project, designed and carried out experiments, analyzed data, visualized data and wrote the final manuscript; GD: designed and carried out experiments; TO: designed and carried out experiments; JR: performed scRNAseq bioinformatic analysis; KR performed TCGA and scRNAseq bioinformatic analysis; MS: carried out experiments. BG: provided administrative support; MM: curated scRNAseq data; PAG: performed statistical analyses; MZ: performed histological analyses; AS: procured human PDAC samples and edited the final manuscript; CLH: edited the final manuscript; HC: procured the mouse model and edited the final manuscript; SMW: edited the final manuscript; LA: performed experiments and analyses and edited the final manuscript; AM: supervised the project, procured funding and edited the final manuscript.

Disclosures:

A.M. receives royalties for a pancreatic cancer biomarker test from Cosmos Wisdom Biotechnology, and this financial relationship is managed and monitored by the UTMDACC Conflict of Interest Committee. A.M. is also listed as an inventor on a patent that has been licensed by Johns Hopkins University to ThriveEarlier Detection. A.M. serves as a consultant for Freenome and Tezcat Biotechnology. All other authors are free of conflicts of interest and have nothing to disclose.

GEO accession number: GSE188946

Background—*RNF43* is an E3 ubiquitin ligase that is recurrently mutated in pancreatic ductal adenocarcinoma (PDAC) and precursor cystic neoplasms of the pancreas. The impact of *RNF43* mutations on PDAC is poorly understood and autochthonous models have not been sufficiently characterized. In this study we describe a genetically engineered mouse model (GEMM) of PDAC with conditional expression of oncogenic *Kras* and deletion of the catalytic domain of *Rnf43* in exocrine cells.

Methods—We generated *Ptf1a-Cre;*LSL-*Kras*G12D;*Rnf43*$^{flox/flox}$ (KRC) *and Ptf1a-Cre;* LSL-*Kras*G12D (KC) mice and animal survival was assessed. KRC mice were sacrificed at 2 months, 4 months and at moribund status followed by analysis of pancreata by single cell RNA sequencing (scRNAseq). Comparative analyses between moribund KRC and a moribund *Kras/Tp53* driven PDAC GEMM (KPC) was performed. Cell lines were isolated from KRC and KC tumors and interrogated by cytokine array analyses, ATAC-seq and *in vitro* drug assays. KRC GEMMs were also treated with an anti-CTLA4 neutralizing antibody with treatment response measured by magnetic response imaging.

Results—We demonstrate that KRC mice display a marked increase in incidence of high-grade cystic lesions of the pancreas and PDAC compared to KC. Importantly, KRC mice have a significantly decreased survival compared to KC mice. By use of scRNAseq we demonstrated that KRC tumor progression is accompanied by a decrease in macrophages, as well as an increase in T and B lymphocytes with evidence of increased immune checkpoint molecule expression and affinity maturation, respectively. This was in stark contrast to the tumor immune microenvironment observed in the KPC PDAC GEMM. Furthermore, expression of the chemokine, CXCL5, was found to be specifically decreased in KRC cancer cells by means of epigenetic regulation and emerged as a putative candidate for mediating the unique KRC immune landscape.

Conclusions—The KRC GEMM establishes *RNF43* as a *bona fide* tumor suppressor gene in PDAC. This GEMM features a markedly different immune microenvironment compared to previously reported PDAC GEMMs and puts forth a rationale for an immunotherapy approach in this subset of PDAC cases.

Graphical Abstract

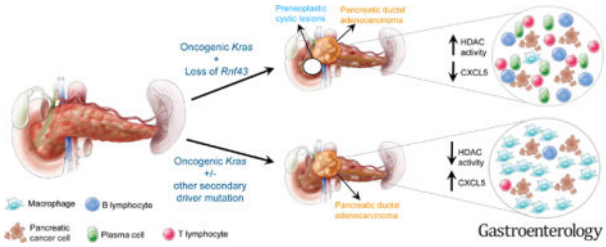

Lay summary:

We report a novel preclinical mouse model of pancreatic cancer featuring loss of the gene *Rnf43*. The unique immune cell composition observed in these tumors raises the possibility of immunotherapy-based approaches in *RNF43* mutated pancreatic cancer.

Keywords

pancreatic cancer; genetically engineered mouse models; single cell RNA sequencing; tumor suppressor gene; KRAS

Introduction:

Pancreatic ductal adenocarcinoma (PDAC) is the third leading cause of cancer-related deaths in the United states, and an estimated 48,220 people will succumb to the disease in 2021 [1]. The incidence of PDAC is on the rise, and PDAC is projected to become the second most common cause of cancer death in the USA by 2030 [2]. As a result, precision-based therapies are needed to address this growing public health problem. To that end, whole exome and whole genome sequencing efforts have revealed a compendium of recurrent mutations in human PDAC [3]. Specifically, 5–10% of resected PDAC cases display loss of function mutations in Ringer Finger Protein 43, *RNF43* [3] In addition, *RNF43* has been shown to be one of the most commonly mutated genes in PDAC precursor, pancreatic cystic neoplasms; including intraductal papillary mucinous neoplasms (IPMN) where it is mutated in approximately half of all cases [4].

RNF43, an E3 ubiquitin ligase enzyme, uses a ring finger domain to catalyze the final step of protein ubiquitination; notably, it has been demonstrated to ubiquitinate Frizzled receptors at the plasma membrane and, in doing so, acts as a negative regulator of Wnt signaling [5]. Recently, preclinical models have demonstrated targeted vulnerability of *RNF43* mutated human PDAC cell lines to blockade of specific Frizzled receptors [6] and small molecule porcupine inhibition, an enzyme critical to the production of functional Wnt ligands [7]. Despite these promising preclinical findings, however, a phase 1 clinical trial of the porcupine inhibitor, WNT974, in *RNF43* mutated solid cancer patients did not display any signal of activity [8]. As such, improved preclinical models of *RNF43* mutated PDAC are needed, to better elucidate how this mutation impacts *Kras*-induced pancreatic neoplasia, and further, for the development of precision-based therapeutics for this subset of patients.

In this report we describe a genetically engineered mouse model (GEMM) of PDAC driven by oncogenic *Kras* and loss of the ring finger domain of *Rnf43*. We demonstrate that *Rnf43* is indeed a *bona fide* tumor suppressor gene in PDAC, as its conditional deletion cooperates with oncogenic *Kras* to increase the incidence of high-grade cystic lesions and subsequent PDAC. Remarkably, we also show that loss of *Rnf43* leads to a distinct tumor immune microenvironment (TIME), characterized by the preponderance of adaptive immune cells at the expense of immunosuppressive myeloid cells, when compared to the prototypal *Kras;Tp53* (KPC) driven PDAC GEMMs with intact *Rnf43* function. This characteristic TIME in the setting of *Rnf43* mutations open up the possibility of utilizing immune checkpoint inhibitors as a potential therapeutic strategy in this subset of patients, in a disease which is essentially recalcitrant to immunotherapy. This study reiterates the importance of autochthonous organisms in identifying therapeutic dependencies that might otherwise not be uncovered in an *ex vivo* or hetero-transplant model.

Materials and Methods:

Generating conditional mice with pancreas-specific Rnf43 deletion

Rnf43$^{fl/fl}$ mice were obtained from Dr. Hans Clevers (Hubrecht Institute, Netherland), and have been previously described [5]. *Rnf43*$^{fl/fl}$ mice were crossed with the embryonic pancreatic epithelium restricted *Cre* recombinase strain, *Ptf1a-Cre*, or the derivative *Ptf1a-Cre;LSL-Kras*^{G12D} mice (KC) to generate *Ptf1a-Cre;Rnf43*$^{fl/+}$, *Ptf1a-Cre;Rnf43*$^{fl/fl}$, *Ptf1a-Cre;Kras*^{G12D}*;Rnf43*$^{fl/+}$ (KRC^{het}) and *Ptf1a-Cre,Kras*^{G12D}*;Rnf43*$^{fl/fl}$ (KRC) mice. We also crossed KC mice to *Tp53*$^{R172H/+}$ mice to obtain *Ptf1a-Cre;Kras*^{G12D}*Tp53*$^{R172H/+}$ (KPC) mice [9]. Mice were maintained in C57BL/6 and DBA/2 genetic backgrounds. All mice were housed in pathogen–free barrier facility with food and water *ad libitum*. Animal studies were conducted in compliance with Institutional Animal Care and Use Committee (IACUC protocol number: 00001222-RN02) guidelines of University of Texas MD Anderson Cancer Center. American Veterinary Medical Association Guidelines for the Euthanasia of Animals were strictly followed

Tissue digestion, single-cell cDNA library preparation and sequencing.

Tumors and pancreas were enzymatically digested into a single-cell suspension precisely as we have previously described [10]. scRNAseq library generation was performed using the 10X Chromium System (10X Genomics Inc; Pleasanton, CA). Single cell suspensions were resuspended in PBS containing 0.04% *w/v* bovine serum albumin and brought to a concentration of 200–700 cells/μL. Appropriate volume of cells was loaded with single cell 5' gel beads into a single cell chip and run on the Chromium Controller (10x Genomics, Inc; Pleasanton, CA). Dynabeads MyOne Silane magnetic beads (Thermo Fisher Scientific) were used to clean up the gel bead emulsion reaction mixture. Full-length, barcoded cDNA was amplified by PCR after cleanup. All samples were run on Agilent Tapestation 4200 using DNA high sensitivity D5000 tape. During library preparation, sample index and Illumina adapter sequences (Illumina Inc; San Diego, CA) were added. After library preparation quality control was performed using DNA D1000 tape on the Agilent Tapestation 4200 and final concentration was measured using the Qubit 4 Fluorometer DNA HS assay (Thermo Fisher Scientific). All samples were loaded at a concentration of 1.5 pM and run on the Illumina NextSeq500 High Output Flowcell. The run configuration was 26 base pairs (bp) × 98 bp × 8.

Single cell RNA-seq analysis

scRNAseq data were analyzed as we had previously described [10]. Cell Ranger version 3.0.2 (10X Genomics) was used to process raw sequencing data. After sequencing and data processing scRNAseq datasets for each time point were computationally pooled for each time point. Individual cells from each time point were then displayed on a respective UMAP plot. Downstream analyses were carried out using Seurat (10X Genomics). KPC and KPfC data sets were obtained from our previously published report [10]. All scRNAseq data produced are to be deposited on the Gene Expression Omnibus platform (https://www.ncbi.nlm.nih.gov/geo: GSE188946)

GEMM antibody treatment

Six month old KRC mice were enrolled onto the anti CTLA-4 treatment trial and treated with either anti-CTLA4 antibody (clone 9H10; Bio X Cell, Lebanon, NH) or *InVivoPlus* Syrian hamster IgG isotype control antibody (Cat# BP0087; Bio X Cell). All antibodies were diluted in *InVivoPure*™ pH 7.0 Dilution Buffer (Bio X Cell). Mice were randomized and treated with 250 μg of antibody, twice per week by intraperitoneal injection.

Orthotopic implantation

Littermates of the mice used for KRC cell line generation were used for orthotopic implantation. At approximately 4 months of age, mice were anesthetized with inhaled isoflurane followed by externalization of the pancreas. 10^5 or 10^6 KRC cell (CXCL5 over expressing or empty vector containing) were resuspended in 50μl Matrigel™ solution (1:1 dilution with phosphate buffered saline) (Corning Inc; Corning, NY) and injected into the body of the pancreas. The pancreas was returned to the abdomen and the fascia and abdominal wall were sutured. Buprenorphine analgesia was used. Mice were monitored daily for signs of distress or excessive weight loss. All mice were sacrificed at 4 weeks and pancreata weighed, fixed in 10% buffered formalin and paraffin embedded.

ATAC-seq Analysis

ATAC-seq was performed following the Omni-ATAC protocol as previously described [11]. Briefly, live cells in culture were washed with phosphate buffered saline followed by harvesting and counting. Nuclei were isolated from approximately 50,000 cells in lysis buffer containing 0.1% NP-40 and 0.01% Digitonin and were fragmented with Nextera Tn5 Transposase (TDE1, Illumina) in TD Tagment DNA buffer (Illumina) for 30 minutes at 37 °C. The resulting library fragments were purified using a Qiagen MinElute kit. Libraries were further amplified 4–6 PCR cycles and purified using AMPure XP beads (Beckman Coulter). ATAC-seq libraries were subsequently sequenced 2 × 75 bp on an Illumina NextSeq500.

Results:

Deficiency of *Rnf43* accelerates the development of *Kras*-driven precursor lesions

To investigate the role of *Rnf43* in pancreatic cancer development, we crossed mice bearing *Ptf1a-Cre* and LSL-*Kras*^{G12D} alleles with those bearing *Rnf43*^{flox} alleles to generate compound progeny with pancreas specific mutant *Kras* expression, and either a heterozygous (KRC^{het}) or bi-allelic loss of *Rnf43* in the pancreas (KRC) (Supp Figure 1A). *Cre*-mediated recombination of *LSL-Kras*^{G12D} allele in the mouse pancreas activates oncogenic *Kras*, which is sufficient to develop pancreatic precursor lesions, and in a subset, results in adenocarcinomas [12]. By nine weeks of age, both KRC^{het} and KRC mice developed enlarged pancreata (Supp Figure 1B), greater areas of acinar parenchyma loss (Supp Figure 1C, D), and greater expression of SOX9 (ductal marker) (Supp Figure 2A) and Ki67 staining (proliferation marker) (Supp Figure 2B, C) in comparison to age matched KC mice

Regarding the role of *Rnf43* in pancreatic development and tumorigenesis, we noted that loss of *Rnf43* is dispensable for normal pancreas development as pancreas specific loss of *Rnf43* in the absence of an activating *Kras* mutation (RC^{het} or RC mice) resulted in normal gross and histological morphology of pancreatic tissue (Supp Figure 3A, B). Moreover, immunohistochemical (IHC) analyses of amylase showed mature acinar cell architecture, while IHC for glucagon and insulin also demonstrated no abnormalities in islets cells (Supp Figure 3B). Pancreatic weight:body ratios were equivalent across KC, RC^{het} and RC mice (Supp Figure 3C) at 9 weeks of age. Importantly, during the course of observation, up to the age of 62 weeks of age, none of the RC^{het} or RC mice developed pancreatic neoplasia (Supp Figure 3D). These data indicate that loss of *Rnf43* is dispensable for pancreas development and requires the presence of oncogenic *Kras* in order to initiate pancreatic neoplasia.

Loss of *Rnf43* cooperates with oncogenic *Kras* in development of murine cystic precursor lesions.

RNF43 is recurrently mutated in mucinous cystic precursor lesions of the pancreas in humans, and most also harbor concurrent oncogenic *KRAS* mutation [13]. Histological examination of pancreatic tissue of mice below the age of 52 weeks (including timed necropsy and survival cohorts), demonstrated significantly higher prevalence of cystic precursor lesions resembling IPMNs in KRC mice (41%) compared to KRC^{het} mice (15%) and KC mice (5%) (Figure 1A–B). Both branch and main duct IPMN lesions were observed whereas mucinous cystic neoplasms were not observed in this GEMM. KRC mice developed high grade cystic precursor lesions as early as nine weeks, a finding not observed in either KC or KRC^{het} (Supp Figure 4A), while both KRC^{het} and KRC demonstrated a significant increase in low grade cystic lesions compared to KC mice at nine weeks old (Supp Figure 4B). Pancreatic cystic lesions were appreciated on gross morphology and recapitulated cystic histology seen in human IPMN (Supp Figure 4C). By five months of age, both KRC^{het} and KRC demonstrated an increase in the incidence of high-grade lesions relative to pancreata from the KC cohort (Supp Figure 4D, E). These data demonstrate the ability of *Rnf43* loss in the KRC GEMM to cooperate with *Kras* in producing cystic lesions of the pancreas akin to *RNF43* loss of function mutations in human patient cohorts.

Pancreas specific loss of Rnf43 cooperates with oncogenic *Kras* to mediate the development of pancreatic adenocarcinoma and decrease survival.

To determine the phenotypic impact of *Rnf43* loss in the context of oncogenic *Kras*, we analyzed the incidence of PDAC in mice of the 3 different genotypes. Overall, we observed a higher incidence of invasive cancer in timed necropsies until 52 weeks of age in KRC^{het} and KRC pancreata compared to KC mice (Figure 1C, D). From our histological analyses of the resulting KRC^{het} and KRC PDAC, we could not delineate with certainty if the PDAC arose from a pre-existing cystic precursor, although we did observe invasive adenocarcinomas even in pancreata with no obvious residual cystic lesions. Notably, *RNF43* mutations are identified in “conventional” human PDAC, without associated IPMNs or MCNs [3], which is consistent with our findings. We also evaluated our cohorts to determine the status of metastatic lesions across different genotypes: 40% of PDAC harboring KC mice were found to have metastases, 50% of KRChet mice and 50% of KRC mice. Of note, all cases of metastatic disease in KRC mice could be observed on gross analyses

(Supp Figure 5A) T2 weighted MRI was capable of detecting these metastatic lesions (Supp Figure 5B). Finally, we performed survival analyses in cohorts of KC, KRC^{het} and KRC mice in which mice were euthanized when they became moribund. Kaplan-Meier survival analysis revealed a significant reduction in survival accompanied by loss of one or both *Rnf43* alleles, with a median survival of 37 weeks for both the homozygous KRC mice and heterozygous KRC^{het} mice compared to 49 weeks for *Rnf43* wild type KC mice (Figure 1E). Lastly, as part of our initial characterization of this novel GEMM we performed contrasted magnetic resonance imaging (MRI) of the moribund KRC GEMM and moribund KPC (*Ptf1a-Cre;Kras^{G12D}*Tp53$^{R172H/+}$) GEMM, whose genotype represents the majority of PDAC patients [3, 9]. On T2 weighted MRI intra-tumoral septations were readily appreciated in the cystic-solid KRC GEMM (Supp Figure 6A, B) whereas the solid KPC GEMM (Supp Figure 6C, D) featured a hazier and less well delineated tumor.

Single cell RNA-seq profiling of the KRC GEMM reveals progression toward a myeloid-low, lymphocyte-rich microenvironment.

Single-cell RNA-sequencing (scRNAseq) was performed on freshly harvested KRC GEMM pancreata, in order to deeply interrogate alterations in the tumor microenvironment from early stages of disease to moribund status. The single-cell suspensions of KRC pancreata were analyzed by the 10X Genomics platform at an early stage (2 months, n=2), an intermediate stage (4 months, n=2), and moribund status (6–10 months, n=3). “Early” KRC (Figure 2A, left), “intermediate” KRC (Figure 2A, center) and “moribund” KRC (Figure 2A, right) contained 2774, 5488 and 3249 cells, respectively. For each UMAP, graph-based population delineation was performed and populations were assigned an identity based on lineage markers we and others have previously employed in assigning cell populations in PDAC GEMMs (Figure 2B) [10, 14]. Percentages of each cell type in each of the three time points were then summarized (Figure 2C).

We observed a diminishing percentage of fibroblasts during KRC progression, with fibroblasts comprising 12.3% of cells in early KRC, 10.3% of cells in intermediate KRC and 2.4% of cells in moribund KRC. This is a similar pattern as we previously observed in an oncogenic *Kras*/*Ink4a* loss driven PDAC GEMM (KIC), where the early time point featured greater than 3 times as many fibroblasts as the moribund time point by cellular percentage [10]. We then interrogated the KRC GEMM fibroblast populations in greater detail by collating and displaying the fibroblasts from each of the early, intermediate and moribund experiments on a single fibroblast UMAP (Figure 2D). We delineated the fibroblast populations based on scRNASeq expression clusters and noted the presence of a *Pi16*$^{+}$/*Fbn1*$^{+}$ expressing population (Fibroblast 1; FB1), a *Cxcl14*$^{+}$/*Ptn*$^{+}$ expressing fibroblast population (Fibroblast 2; FB2) and a *Cav1*$^{+}$/*Msln*$^{+}$/*Cd74*$^{+}$ expressing fibroblast population (Fibroblast 3; FB3) (Supp Figure 7A), reproducing the same three fibroblasts subtypes we had previously described [10]. In contrast to the presence of all three fibroblast subtypes in early and intermediate KRC, we noted that nearly all the KRC moribund fibroblasts belonged to only two distinct subpopulations; FB1-iCAF and FB1myCAF-like [15], both of which had retained *Pi16*$^{+}$/*Fbn1*$^{+}$ expression with no appreciable *Cxcl14*$^{+}$/*Ptn*$^{+}$ expression (Figure 2E). Indeed, we had previously reported that all three fibroblast populations are present in normal mouse pancreas and early PDAC GEMMs, but FB2 fades

by the moribund stage in two different PDAC GEMMs [10]. Moreover, in addition to *Pi16*$^{+}$/*Fbn1*$^{+}$ expression, the FB1-iCAF population expressed several inflammatory cytokines (examples: *Il6* and *Ccl7*), similar to the inflammatory cancer associated fibroblast (iCAF) population, which has recently been described (Supp Figure 7B) [15]. The FB1-myCAF-like population contained *Acta2* and *Tagln* expressing cells, comparable to the myCAF population described by the same investigators. The FB3 population (comparable to apCAF) was present in early KRC and intermediate KRC, consistent with our previous reports in the KIC GEMM [10] however, these cells were greatly diminished by the moribund stage, in conjunction with an overall reduction in the cumulate CAF population.

Myeloid cells were noted to comprise the plurality of cells in the early KRC data set (45.5%) compared to intermediate KRC (15.7%) and moribund KRC experiments (12.3%) where the percentage of myeloid cells was approximately one third of that observed in early KRC (Figure 2A–C). Conversely, the early KRC GEMM contained only 10.6% cells as T cells whereas this percentage was greater than doubled in the intermediate (23.2%) and moribund (21.4%) KRC GEMMs. Importantly, we also noted a significant increase in T-cells present in *RNF43* human PDAC samples in comparison to *RNF43* wild type human PDAC samples (Supp Figure 8A). Most prominent was the expansion of the B cell lineage during KRC progression, which increased from KRC early (6.8%), to KRC intermediate (29.8%) and finally KRC moribund (40.9%). Consistent with this B cell expansion during KRC progression, we observed the emergence of a readily discernible plasma cell population by the KRC moribund stage which comprised ~15% of cells. Together, B cell lineage (B lymphocytes + plasma cells) comprised greater than half of all cells by cellular percentage in the moribund KRC GEMM scRNAseq dataset (Figure 2A, C). The intermediate KRC time point also noted the emergence of a population of myeloid-derived suppressor cells (MDSCs; ~1%), which overexpressed *S100A8*, *S100A9* and *G0s2*, and expanded to 2.2% by the KRC moribund stage.

The immune composition observed in the moribund KRC GEMM featured a low myeloid:lymphocyte ratio and represents the inverse of the scenario we previously described in moribund KPC GEMM which featured a high myeloid:lymphocyte ratio (Supp Table 1). Interestingly, whereas we report a median survival of 37 weeks for the KRC GEMM, the previously published median survival of the *Kras/Tp53* driven PDAC GEMMs is 12–20 weeks [16]. This survival discrepancy may, at least in part, be due to the decreased myeloid cells and increased lymphocytes seen in the KRC GEMM.

KRC GEMM progression is accompanied by a decrease in inflammatory macrophages and preservation of monocytes and dendritic cells in the TIME

We next performed a focused myeloid lineage analysis, compiling all myeloid cells from the three stages of KRC GEMM progression and displaying them on a single UMAP plot (Figure 3A, Supp Figure 9A). These analyses revealed the presence of three distinct populations of dendritic cells; conventional dendritic cell 1 (cDC1) cells, which specifically expressed *Itgae, Irf8, Flt3, Clec9a, Xcr1*; second, cDC2 cells, which expressed *Cd209a*, and third a primed population of cDC1 cells (cDC1'), which like cDC1 expressed *Irf8* and *Flt3* but also expressed *Ccr7* and *Ccl5*. The latter are markers of cDC1 cells that have been

primed by antigen in regional lymph nodes and has been described in the KPC GEMM [17]. Monocyte and macrophage cell populations were subsequently defined in the KRC GEMM. Importantly, in the KPC GEMM, it has been previously reported that embryonal derived, pancreatic tissue resident macrophages, expand during PDAC progression, and have pro-tumorigenic properties, while a monocytic population is recruited from the bone marrow during tumorigenesis and has a role in antigen presentation [18]. In our KRC scRNAseq data we assigned myeloid population identities based on previously described cell type markers [10, 14] and observed the presence of a large macrophage population that was comprised of 3 macrophage subpopulations. These macrophages were rich in inflammatory molecules such as *Ccl6, Il6* and the complement molecules *C1qa* and *C1qb*. Specifically, subpopulation 1 overexpressed the tissue resident macrophage marker *Adgre1* (F4/80), in addition to other inflammatory markers such as *Apoe*, *Pf4* and *Ccl3*. Of note, we observed a distinct *Cd14*$^{+}$/*Thbs1*$^{+}$ monocyte population.

We then applied KRC stage to the myeloid lineage UMAP to determine if the prevalence of different myeloid cell types change during KRC GEMM progression (Figure 3B). Remarkably, we noted a substantial diminishment of pro-inflammatory/tissue resident macrophages in the KRC moribund stage, where these cells comprised only 11.5% of all myeloid cells, in comparison to the KRC early and intermediate stages where they comprised as much as 73.3% and 73.5% of all myeloid cells, respectively (Figure 3C). Monocytic cells and all 3 populations of dendritic cells were present across the 3 KRC GEMM stages making the marked decrease in tissue resident/inflammatory macrophages in the KRC moribund stage largely responsible for the overall marked reduction of myeloid cells in the moribund stage (Figure 3C). We also performed a comparative analysis of scRNAseq data of myeloid cell distribution from KRC moribund mice compared with myeloid cell distribution from moribund KPC mice we had previously reported [10]. By collating the myeloid cells from these two GEMMs (Supp Figure 9B) we observed a population of *Adgre1+* tissue resident macrophages in the KPC GEMM which is essentially devoid in the moribund KRC tumors (Figure 3D). We also noted a decrease in expression of inflammatory cytokines in KRC macrophages in comparison to KPC macrophages (Supp Fig 9C). We confirmed the marked decrease in F4/80^{+} (*Adgre1*) macrophages in KRC tumors relative to KPC tumors by multi-color immunofluorescence (Figure 3E, F; Supp Figure 10, 11). The noticeable divergence in myeloid cell composition in moribund KRC *versus* KPC mice underscores the influence of *Kras* cooperating mutations in framing the respective TIME, and the possibility of leveraging this unique milieu for therapeutic benefit.

Focused B-cell lineage analysis reveals expansion and clonal maturation of B cells during KRC progression

We pooled all B-cell lineage cells (B-cells and plasma cells) from the KRC early, intermediate and moribund experiments and displayed them on a single UMAP (Figure 4A). This analysis resulted in the segregation of cells into 3 distinct groups; B cells, early plasma cells (1 subgroup) and mature plasma cells (2 subgroups). As expected, based on previous analyses (Figure 2), when the KRC stage identity was applied we noted that nearly all the plasma cells were derived from the KRC moribund stage (Figure 4B). Moreover, the early KRC B-cells were positioned toward the bottom of the UMAP with

intermediate and ultimately moribund KRC B-cells showing a pseudo-trajectory toward regions of the plot in closer proximity to the plasma cells. We also performed clustering analyses using expression values of all significant immunoglobulin transcripts in the 3 subpopulations of plasma cells (Figure 4C). Theses analyses illustrated the specific over-expression of 2–3 immunoglobulin genes in each of the mature plasma cells subpopulations. Both mature plasma cell populations specifically over-expressed at least one variable heavy chain immunoglobulin gene and one variable light chain immunoglobulin gene. This is in contrast to the early plasma cell population which overexpressed *Jchain* and *Ighm*, which are markers of an early humoral response [19]. These data were also illustrated with single gene UMAPs of a gene specific for each of the late plasma cell and the early plasma cell populations (Figure 4D). When all B-cell lineage derived cells from the KRC moribund and KPC moribund GEMMs were collated on a single UMAP, we observed only a few cells in the main B lymphocyte population, in addition to the early plasma cell population, that were derived from the KPC mice, while the late plasma cell populations were almost entirely derived from the KRC tumors (Supp Figure 12A, B). Taken together, these data indicate that, in sharp contrast to the KPC GEMM, disease progression in the KRC GEMM is uniquely accompanied by the expansion and maturation of an adaptive B-cell response, culminating in clonal plasma cells which have likely undergone affinity maturation.

Focused T cell analysis of the KRC GEMM reveals regulatory T-cell immune checkpoint molecule upregulation as a potential mechanism of immune evasion during KRC progression.

To further interrogate the temporal composition of the KRC TIME, all T-cells from the early, intermediate and moribund KRC scRNAseq datasets were projected on a single, T-cell focused, UMAP (Figure 5A). Graph based population delineation identified commonly described T-cell subsets: naïve T-cells (*Ccr7, Lef1, Dusp10*), activated T-cells (*Cd8*, *Gzma, Gzmb, Ccl5*), regulatory T-cells (Treg) and group 2 innate lymphoid cells (ILC2; *Gata3, Rora, Areg, Il5*) which has recently been shown to have a critical role in mediating PDAC sensitivity to immune checkpoint blockade [20]. We also observed the presence of dysfunctional T-cells that express *Id2, Cd8, Cd8b1*, and have recently been described in other immune checkpoint sensitive solid cancers (melanoma, non-small cell lung cancers) to be a major proliferating immune cell component [21]. When the KRC stage identities were overlayed with the T-cell UMAP (Figure 5B) we noted that the dysfunctional T cell compartment was composed entirely of cells derived from the KRC intermediate stage, indicating a proliferative population as the TIME shifts to a lymphocyte rich state. None of the naïve T-cells, T_{regs} or activated T-cells displayed dominance or depletion of any particular stage during stages of KRC GEMM progression. To investigate potential mechanisms of immune escape in the KRC GEMM we performed a focused analysis on all immune checkpoint or costimulatory genes expressed in the T_{reg} cell population (Figure 5C): *Ctla4, Pdcd1, Icos, Tnfsf4* (OX40)*, Tnfsf8 and Cd83*. These analyses revealed an increase in expression intensity and percent of the T_{reg} population expressing each of these immune checkpoint genes as the KRC GEMM progressed from early to intermediate and moribund stages. A notable exception to this was *Icos* which demonstrated a decrease in expression intensity as the GEMM progressed, which is consistent with the function of ICOS as a co-stimulatory receptor in T-cell activation [22]. In light of this unique T cell

contexture in the moribund KRC mice, we performed a proof-of-concept assay in which KRC mice were treated twice per week with either an anti-CTLA4 blocking antibody (n=6) or an IgG isotype control antibody (n=6), given by intraperitoneal injection for a fixed 24-day duration. CTLA4 was selected given its current clinical use as therapeutic immune checkpoint target in other solid cancers [23] and its increasing expression during KRC progression: *Ctla4* was expressed in 22%, 30% and 53% of early, intermediate and moribund KRC regulatory T-cells, respectively (Figure 5C). KRC mice were enrolled onto treatment at 6 months of age, randomized to one of the two arms and a baseline MRI was performed (Figure 5D). Imaging was repeated halfway through the trial and at the end of the treatment course. The primary endpoint of this assay was progression on imaging or mouse death while on treatment. During this trial, 4/6 mice in the IgG isotype treated group died while 2/6 mice in this group showed progression on imaging; all mice in this arm met the primary endpoint (Figure 5E, F). In contrast, 4/6 mice in the anti-CTLA4 antibody treated group experienced radiographic stability and 2/6 mice experienced a radiographic response; none of the mice in this arm met the primary endpoint. Treatment with anti-CTLA4 antibody resulted in an approximately 5-fold increase in numbers of intratumoral T cells compared to isotype control antibody treated KRC mice (Supp Figure 13A).

Cxcl5 is decreased in KRC cancer cells and is a putative mechanism for KRC indolence and its distinct TIME

To understand the basis for the unique TIME observed in KRC mice versus prototypal KPC tumors, we sought to determine if KRC cancer cells differentially expressed paracrine signals, relative to *Rnf43* intact mouse PDAC cell lines, which could play a role in mediating the observed immune landscape. To that end, conditioned media from two murine cell lines derived from moribund KRC tumors *versus* two murine cell lines derived from *Rnf43* intact PDAC cell lines were compared using multiplex mouse cytokine arrays (Figure 6A). In this 2 × 2 cell line analysis only one secreted factor was consistently different between the two groups; CXCL5 was decreased in the KRC cell lines relative to the *Rnf43* intact cell lines. We then confirmed this finding by use of ELISA on the conditioned media and added a third cell line for each group (Figure 6B). Quantitative PCR analysis was performed on these cell lines with concordant results indicating a potential transcriptional mechanism for low CXCL5 ligand levels in KRC cell lines (Figure 6C). Moreover, we compared *Cxcl5* expression in the cancer cell population of KPC and KRC scRNAseq datasets and confirmed low gene expression *in vivo* in the KRC GEMM compared to the KPC GEMM (Figure 6D). Notably, in our KRC scRNAseq dataset, the only cell population that expressed the CXCL5 receptor, CXCR2, was a population of MDSCs which first appeared in the KRC intermediate stage and expanded in the KRC moribund stage (Figure 2A, B). *Cxcr2* expression was noted in the MDSC population of both KRC and KPC GEMMs (Supp Figure 14). We also compared *CXCL5* gene expression level in a cohort of laser capture microdissected human IPMN samples concurrently profiled for *RNF43* mutation and expression, and found that expression was indeed lower in *RNF43* mutated patient samples (Supp Figure 8B). In order to understand the transcriptional mechanism whereby *Cxcl5* expression is decreased in KRC cells we performed ATAC-seq analysis which revealed a marked decrease in chromatin accessibility in the regions flanking the transcription start site of *Cxcl5* in KRC cell lines relative to the *Rnf43* intact PDAC cell lines (Figure 6E).

Given the decreased chromatin accessibility at the *Cxcl5* regulatory regions in KRC cell lines we asked if it would be possible to increase *Cxcl5* expression in KRC cell lines by inhibiting histone deacetylates (HDAC). Indeed, treatment with the pan-HDAC inhibitor, panobinostat, resulted in a dose dependent increase in *Cxcl5* expression in KRC cell lines with 22–173-fold change in *Cxcl5* gene expression at the 50nM treatment dose versus the vehicle control (Figure 6F). Furthermore, to determine the role of decreased *Cxcl5* expression in the KRC GEMM we employed lentiviral transduction to stably over-expressed *Cxcl5* in KRC cell lines, resulting in protein levels comparable to that observed in the *Rnf43* intact PDAC cell lines. We then orthotopically implanted 10^5 KRC-*Cxcl5* overexpressing cells or 10^5 KRC-empty vector transduced cells in the pancreas of littermate mice resulting in an immunocompetent orthotopic mouse model. At the end of the study, we noted that the *Cxcl5* overexpressing KRC cell line resulted in pancreas weights >3-fold than those observed in the empty vector transduced KRC cell line (Figure 6G). Importantly, no notable tumor growth on the MRIs of the empty-vector transduced orthotopic injections were observed whereas clear tumors were observed in the *Cxcl5*-overexpressing KRC cell line orthotopic implants (Figure 6H). Additionally, over-expression of *Cxcl5* in orthotopically implanted KRC cell lines resulted in increased macrophages (F4/80 positivity), with similar F4/80 positivity to the KC GEMM (Supp Figure 13B, C). We also increased the number of implanted cells to 10^6 and noted persistent increase in tumor incidence and pancreas weight in the *Cxcl5* overexpressing tumors in comparison implants with vector transduced cells (Supp Figure 13C, D, E).

Discussion

In this study, we provide rigorous *in vivo* validation that *Rnf43* is a *bona fide* tumor suppressor gene in PDAC, and that it cooperates with mutant *Kras* in accelerating the development of IPMN-like precursor cystic lesions, as well as invasive adenocarcinomas, thus recapitulating the cognate multistep process observed in humans. Notably, KRC^{het} mice, which featured loss of only one *Rnf43* allele, had a decreased survival equivalent to the KRC mice harboring loss of both *Rnf43* alleles. This observation suggests that haploinsufficiency, and therefore a decreased *Rnf43* gene dosage, may be sufficient to drive the phenotype we observed in this study. Indeed, in previously sequenced human PDAC samples, *RNF43* mutated tumors demonstrated an alteration at only one copy of *RNF43* with the other copy remaining intact, while 90% of *RNF43* mutated patients also featured mutations in either *TP53* or *SMAD4* [3]. We observed that both the KRC^{het} and KRC cancer epithelium displayed increased Wnt activity which was reversed by a Wnt inhibitor despite demonstrating insensitivity the Wnt inhibitor (Supp Figure 15). Indeed, in a recent phase 1 clinical trial of a novel porcupine inhibitor in advanced solid tumors, including *RNF43* mutated PDAC, 0/94 patients experienced a response [8]. Further investigations of the KRC and KRC^{het} cancer epithelium will be required to understand the mechanisms by which even monoallelic *Rnf43* loss promotes the transformation to neoplastic epithelium in the presence of oncogenic *Kras*.

The most conspicuous feature of the KRC GEMM reported in this study is the unique TIME we observed during KRC progression. At the KRC early time point we observed that myeloid cells were the most abundant cell type with lymphocytes comprising only a

minority of cells. However, over the course of KRC progression from early to intermediate and moribund status, the myeloid:lymphocyte composition reversed, such that the majority of cells were of lymphocyte lineage by the moribund stage. Specifically, we noted a substantial increase in lymphocyte lineage cells at the KRC moribund stage where they comprised greater than three quarters of all cells in comparison to the KPC tumors, where lymphocytes cumulatively made up only 2.5%–18.5% of cells at this stage [10]. In addition, previous scRNAseq analyses of KPC have shown that myeloid cells comprise the majority of cells in moribund mice [10, 14]. In contrast, while most myeloid cells in the early and intermediate KRC stages were tissue resident and inflammatory macrophages, these cells were markedly diminished by the KRC moribund stage. Indeed, tissue resident macrophages have been shown to persist and expand within the pancreas over the lifespan of a mouse and depletion of this macrophage subset results in a marked decrease in tumor size in the KPC GEMM [18]. More specifically, it has been demonstrated in KPC mice that *Adgre1+* macrophages mediate T-cell exclusion from the PDAC microenvironment and that depleting this population of macrophages promoted T-cell tumor infiltration, resulting in tumor regression when combined with a CD40 agonist [24]. A separate study demonstrated that a small molecule inhibitor of CSF1R depleted inflammatory, tissue resident macrophages from the KPC tumor microenvironment and resulted in an improved T-cell response, decreased tumor size and improved animal survival [25]. These studies highlight the role of tissue resident macrophages in contributing towards a pro-tumorigenic, immune suppressive milieu within the PDAC TIME. Indeed, the paucity of tissue resident macrophages observed during KRC progression may contribute to the prolonged survival of the KRC GEMM in comparison to the KPC GEMM [26] and is a hypothesis that requires further exploration in subsequent studies of the KRC GEMM.

The KRC GEMM featured the expansion of early plasma cells (*Jchain*$^{+}$/*Igm*$^{+}$) along with evidence of affinity maturation toward mature plasma cells which had lower *Jchain* expression and specifically expressed several immunoglobulin genes. To our knowledge, this is a unique feature of the KRC GEMM with prototypal published models such as KPC and KIC not displaying the presence of an expanded B cell population and terminally differentiated plasma cell population [10, 14]. Furthermore, in a neoadjuvant immune checkpoint blockade (ICB) treatment trial of melanoma patients, B-cell gene expression signatures were found to be the most differentially expressed genes in the tumors of patients who responded to ICB versus those patients who responded poorly to ICB [27]. Also, in the KRC GEMM the *Ctla4* immune checkpoint gene was found to be overexpressed, in concert with several other immune checkpoint genes, with increasing intensity and frequency in the T_{reg} cell compartment. This study is the first we are aware of which putatively demonstrates an intrinsic ICB sensitivity in a PDAC GEMM as previous studies have repeatedly demonstrated no response to ICB in the standard bearer KPC GEMM [28]. These findings open a potential translational opportunity for ICB in *RNF43* mutated PDAC patients that will need to be validated in clinical trials.

We also identified a pivotal chemokine, CXCL5, which plays a role in mediating the cellular composition of the unique KRC TIME. *Cxcl5* expression was epigenetically regulated and could be increased by HDAC inhibition. These data suggest increasing cancer cell HDAC activity over the course of KRC tumor development which negatively regulates *Cxcl5*

expression. Further studies aimed at dissecting dysregulated HDAC signaling pathways in the KRC GEMM are required. Importantly, CXCL5 is a chemokine which has been shown to be overexpressed in a subset of PDAC tumors and is associated with poor patient survival [29]. Moreover, CXCL5 overexpression in human PDAC has been shown to positively correlate with increased intra-tumoral, immunosuppressive macrophages and neutrophils [30]. We also identified a population of MDSCs which are present in both the KRC and KPC GEMMs and are the only population to express the CXCL5 receptor, *CXCR2* (Supp Figure 14). The role of $CXCR2^+$ MDSCs in the KPC GEMM has previously been explored [31]; small molecule inhibition of CXCR2 resulted in increased intra-tumoral T-cell entry and sensitization to ICB which ultimately prolonged animal survival. Importantly, the KPC GEMM comprised approximately double the MDSC frequency as KRC (Supp Table 1) suggesting that the decreased *Cxcl5* expression in KRC may decrease the number of intratumoral MDSCs. While these data demonstrate that CXCR2 inhibition is a strategy for ICB sensitization in the KPC GEMM, the low expression of the CXCR2 ligand, *Cxcl5*, in the KRC GEMM may render this model intrinsically sensitive to ICB (Supp Figure 16).

The lymphocyte-rich, macrophage-poor TIME seen in the KRC GEMM may, at least in part, begin to explain the observation that while the survival of KRC mice is shorter than KC mice, it is nonetheless improved in comparison to KPC (Supp Table 1) [16]. The impact of *RNF43* mutations on the natural history of PDAC has not been studied in detail. Of note, in the 5–10% of PDAC patients in the TCGA dataset who harbor activating *KRAS* mutations and loss of function *RNF43* mutations, an improved survival is observed compared to *RNF43* wild type cases [32] (Supp Figure 8C). Moreover, in PDAC patients who have undergone curative intent resection, *RNF43* mutation status may uniquely predict for decreased chance of recurrence [33]. Our data provides the underlying rationale to further expand on this observation and further leverage therapeutic dependencies such as susceptibility to immune checkpoint inhibitor therapy to further improve survival in this subset of patients.

Supplementary Material

Refer to Web version on PubMed Central for supplementary material.

Funding Sources:

AM is supported by NIH grants R01 CA220236 and R01 CA218004. AM is also funded by the Sheikh Khalifa Bin Zayed Foundation

References:

1. Siegel RL, et al. , Cancer Statistics, 2021. CA Cancer J Clin, 2021. 71(1): p. 7–33. [PubMed: 33433946]
2. Rahib L, et al. , Projecting cancer incidence and deaths to 2030: the unexpected burden of thyroid, liver, and pancreas cancers in the United States. Cancer Res, 2014. 74(11): p. 2913–21. [PubMed: 24840647]
3. Cancer Genome Atlas Research Network. Electronic address, a.a.d.h.e. and N. Cancer Genome Atlas Research, Integrated Genomic Characterization of Pancreatic Ductal Adenocarcinoma. Cancer Cell, 2017. 32(2): p. 185–203 e13. [PubMed: 28810144]

4. Noe M, et al. , Genomic characterization of malignant progression in neoplastic pancreatic cysts. Nat Commun, 2020. 11(1): p. 4085. [PubMed: 32796935]
5. Koo BK, et al. , Tumour suppressor RNF43 is a stem-cell E3 ligase that induces endocytosis of Wnt receptors. Nature, 2012. 488(7413): p. 665–9. [PubMed: 22895187]
6. Steinhart Z, et al. , Genome-wide CRISPR screens reveal a Wnt-FZD5 signaling circuit as a druggable vulnerability of RNF43-mutant pancreatic tumors. Nat Med, 2017. 23(1): p. 60–68. [PubMed: 27869803]
7. Jiang X, et al. , Inactivating mutations of RNF43 confer Wnt dependency in pancreatic ductal adenocarcinoma. Proc Natl Acad Sci U S A, 2013. 110(31): p. 12649–54. [PubMed: 23847203]
8. Rodon J, et al. , Phase 1 study of single-agent WNT974, a first-in-class Porcupine inhibitor, in patients with advanced solid tumours. Br J Cancer, 2021. 125(1): p. 28–37. [PubMed: 33941878]
9. Hingorani SR, et al. , Trp53R172H and KrasG12D cooperate to promote chromosomal instability and widely metastatic pancreatic ductal adenocarcinoma in mice. Cancer Cell, 2005. 7(5): p. 46983.
10. Hosein AN, et al. , Cellular heterogeneity during mouse pancreatic ductal adenocarcinoma progression at single-cell resolution. JCI Insight, 2019. 5.
11. Corces MR, et al. , An improved ATAC-seq protocol reduces background and enables interrogation of frozen tissues. Nat Methods, 2017. 14(10): p. 959–962. [PubMed: 28846090]
12. Hingorani SR, et al. , Preinvasive and invasive ductal pancreatic cancer and its early detection in the mouse. Cancer Cell, 2003. 4(6): p. 437–50. [PubMed: 14706336]
13. Amato E, et al. , Targeted next-generation sequencing of cancer genes dissects the molecular profiles of intraductal papillary neoplasms of the pancreas. J Pathol, 2014. 233(3): p. 217–27. [PubMed: 24604757]
14. Elyada E, et al. , Cross-Species Single-Cell Analysis of Pancreatic Ductal Adenocarcinoma Reveals Antigen-Presenting Cancer-Associated Fibroblasts. Cancer Discov, 2019. 9(8): p. 1102–1123. [PubMed: 31197017]
15. Ohlund D, et al. , Distinct populations of inflammatory fibroblasts and myofibroblasts in pancreatic cancer. J Exp Med, 2017. 214(3): p. 579–596. [PubMed: 28232471]
16. Guerra C and Barbacid M, Genetically engineered mouse models of pancreatic adenocarcinoma. Mol Oncol, 2013. 7(2): p. 232–47. [PubMed: 23506980]
17. Hegde S, et al. , Dendritic Cell Paucity Leads to Dysfunctional Immune Surveillance in Pancreatic Cancer. Cancer Cell, 2020. 37(3): p. 289–307 e9. [PubMed: 32183949]
18. Zhu Y, et al. , Tissue-Resident Macrophages in Pancreatic Ductal Adenocarcinoma Originate from Embryonic Hematopoiesis and Promote Tumor Progression. Immunity, 2017. 47(2): p. 323–338 e6. [PubMed: 28813661]
19. Castro CD and Flajnik MF, Putting J chain back on the map: how might its expression define plasma cell development? J Immunol, 2014. 193(7): p. 3248–55. [PubMed: 25240020]
20. Moral JA, et al. , ILC2s amplify PD-1 blockade by activating tissue-specific cancer immunity. Nature, 2020. 579(7797): p. 130–135. [PubMed: 32076273]
21. Li H, et al. , Dysfunctional CD8 T Cells Form a Proliferative, Dynamically Regulated Compartment within Human Melanoma. Cell, 2019. 176(4): p. 775–789 e18. [PubMed: 30595452]
22. Solinas C, Gu-Trantien C, and Willard-Gallo K, The rationale behind targeting the ICOS-ICOS ligand costimulatory pathway in cancer immunotherapy. ESMO Open, 2020. 5(1).
23. Yang Y, et al. , Comparative Efficacy and Safety of Nivolumab and Nivolumab Plus Ipilimumab in Advanced Cancer: A Systematic Review and Meta-Analysis. Front Pharmacol, 2020. 11: p. 40. [PubMed: 32116716]
24. Beatty GL, et al. , Exclusion of T Cells From Pancreatic Carcinomas in Mice Is Regulated by Ly6C(low) F4/80(+) Extratumoral Macrophages. Gastroenterology, 2015. 149(1): p. 201–10. [PubMed: 25888329]
25. Candido JB, et al. , CSF1R(+) Macrophages Sustain Pancreatic Tumor Growth through T Cell Suppression and Maintenance of Key Gene Programs that Define the Squamous Subtype. Cell Rep, 2018. 23(5): p. 1448–1460. [PubMed: 29719257]

26. Bardeesy N, et al. , Both p16(Ink4a) and the p19(Arf)-p53 pathway constrain progression of pancreatic adenocarcinoma in the mouse. Proc Natl Acad Sci U S A, 2006. 103(15): p. 5947–52. [PubMed: 16585505]

27. Helmink BA, et al. , B cells and tertiary lymphoid structures promote immunotherapy response. Nature, 2020. 577(7791): p. 549–555. [PubMed: 31942075]

28. Feig C, et al. , Targeting CXCL12 from FAP-expressing carcinoma-associated fibroblasts synergizes with anti-PD-L1 immunotherapy in pancreatic cancer. Proc Natl Acad Sci U S A, 2013. 110(50): p. 20212–7. [PubMed: 24277834]

29. Li A, et al. , Overexpression of CXCL5 is associated with poor survival in patients with pancreatic cancer. Am J Pathol, 2011. 178(3): p. 1340–9. [PubMed: 21356384]

30. Zhang R, et al. , CXCL5 overexpression predicts a poor prognosis in pancreatic ductal adenocarcinoma and is correlated with immune cell infiltration. J Cancer, 2020. 11(9): p. 23712381.

31. Steele CW, et al. , CXCR2 Inhibition Profoundly Suppresses Metastases and Augments Immunotherapy in Pancreatic Ductal Adenocarcinoma. Cancer Cell, 2016. 29(6): p. 832–845. [PubMed: 27265504]

32. McIntyre CA, et al. , Alterations in driver genes are predictive of survival in patients with resected pancreatic ductal adenocarcinoma. Cancer, 2020. 126(17): p. 3939–3949. [PubMed: 32573775]

33. Dreyer SB, et al. , Genomic and molecular analyses identify molecular subtypes of pancreatic cancer recurrence. Gastroenterology, 2021.

What you need to know:

Background and Context:

RNF43 is mutated in 5–10% of human PDAC yet there exists no genetically engineered mouse models (GEMM) to investigate the biology of this mutation and its potential clinical implications.

New Findings:

We demonstrate that pancreas specific loss of function of *Rnf43* cooperates with oncogenic *Kras* to produce cystic lesions, PDAC and decreased survival in a GEMM (KRC). The KRC GEMM features a low myeloid, high lymphocyte tumor microenvironment which is in stark contrast to previously published PDAC GEMMs which may render it susceptible to immune checkpoint blockade. The chemokine *Cxcl5* is downregulated by epigenetic means and is a potential mediator of this unique microenvironment.

Limitations:

These preclinical data will need to be validated in *RNF43* mutated PDAC patients

Impact:

The KRC GEMM is a novel platform for the development of therapeutics in *RNF43* mutated PDAC. Immune checkpoint blockade may represent an initial precision-based approach in these patients.

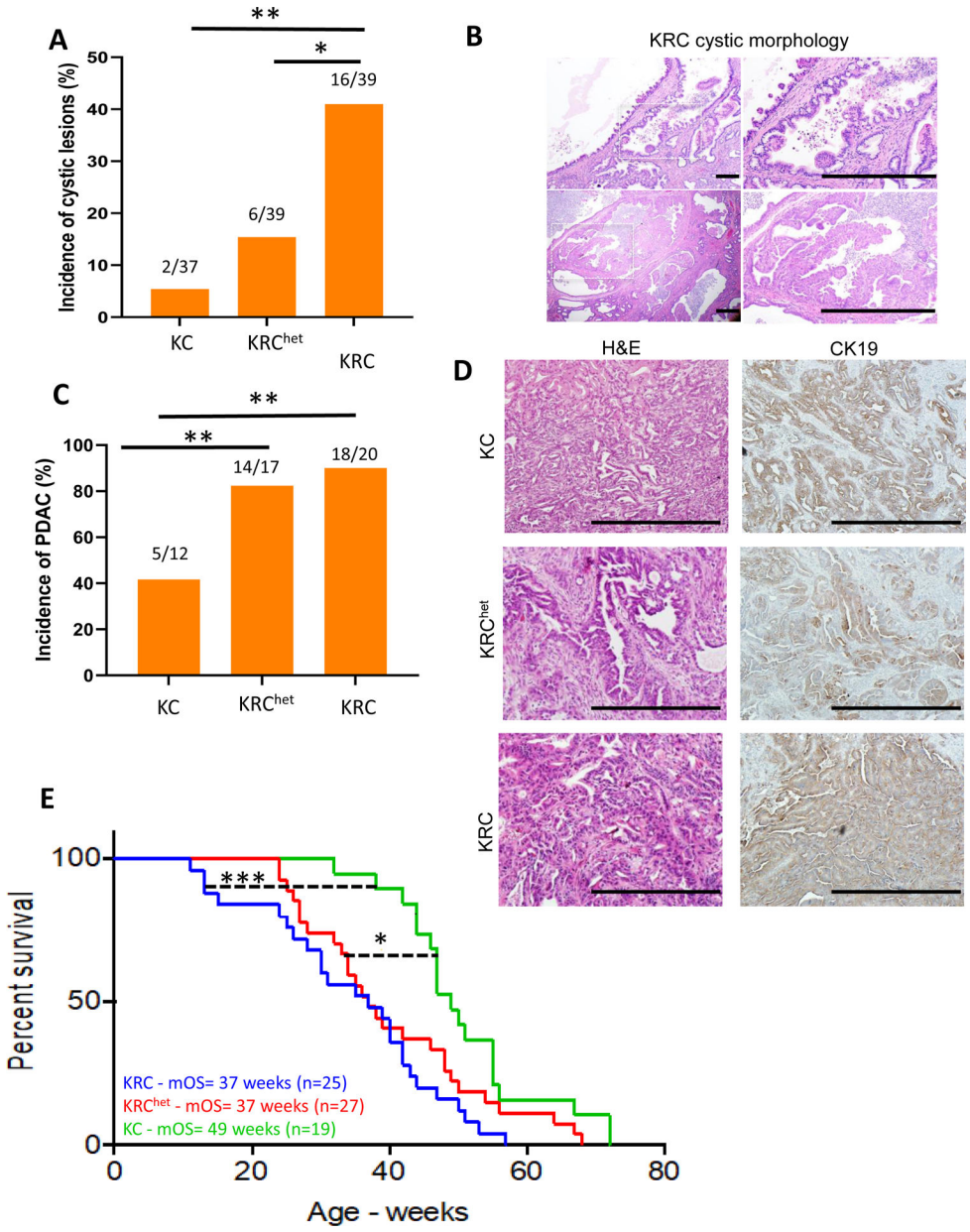

Figure 1: Loss of *Rnf43* cooperates with oncogenic *Kras* in the development of cystic lesions and invasive ductal adenocarcinoma of the pancreas with shortened survival.

(A) Bar graph displaying the incidence of cystic lesions in mice below the age of 52 weeks, including mice from both survival and timed-necropsy cohorts. Two-sided Fisher's exact test was performed to calculate p-value. (B) Representative images of KRC cystic histology showing mucinous papillary projections of ductal epithelium. Black scale bar: 500 μm. (C) Bar graph showing cancer incidences of mice within the age of 52 weeks. Two-sided Fisher's test performed. **p<0.01. (D) Representative images of H&E and CK19 staining of PDAC from indicated genotypes (Black scale bar: 500 μm.). (E) Overall survival analysis of mice with indicated genotypes. Log-rank test was performed (*p <0.05; ***p<0.001).

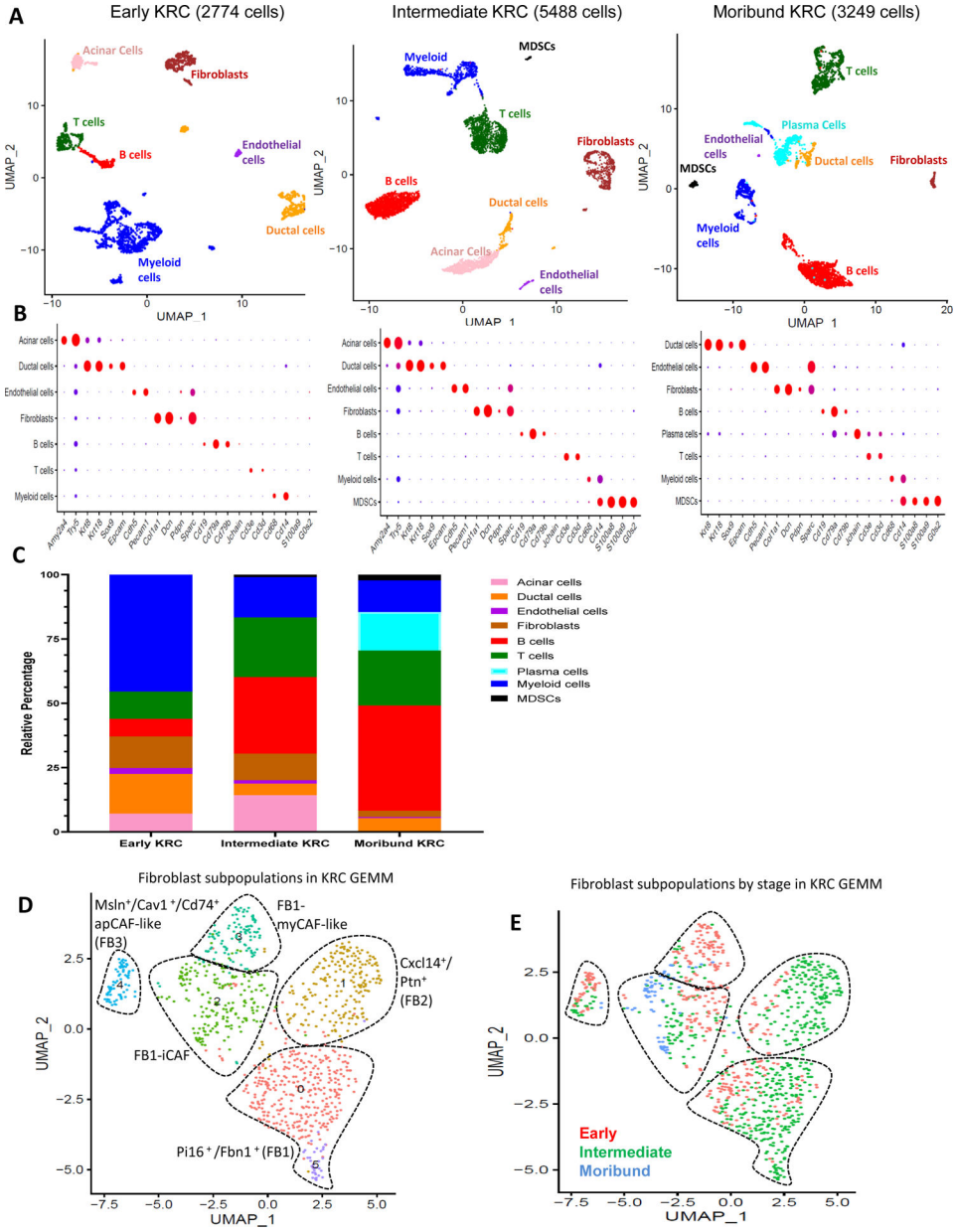

Figure 2: scRNAseq analysis of KRC GEMM progression.

(A) UMAP plots of all cells in the early (left; 2774 cells), intermediate (center; 5488 cells) and moribund (right; 3249 cells) KRC GEMM stages. Cell lineage is labeled and denoted by color on each UMAP plot. (B) Dot plots corresponding to each of the UMAPs; KRC early (left), KRC intermediate (center), KRC moribund (right). C) Summary bar graph denoting the percentage of each cell type observed in the UMAPs for each of the three stages analyzed. Color legend appears in the graphic. D) UMAP displaying all fibroblasts observed across the three KRC stages with a graph-based population delineation method applied to illustrate fibroblast subpopulations. (E) Fibroblast UMAP with each cell color coded according to KRC stage.

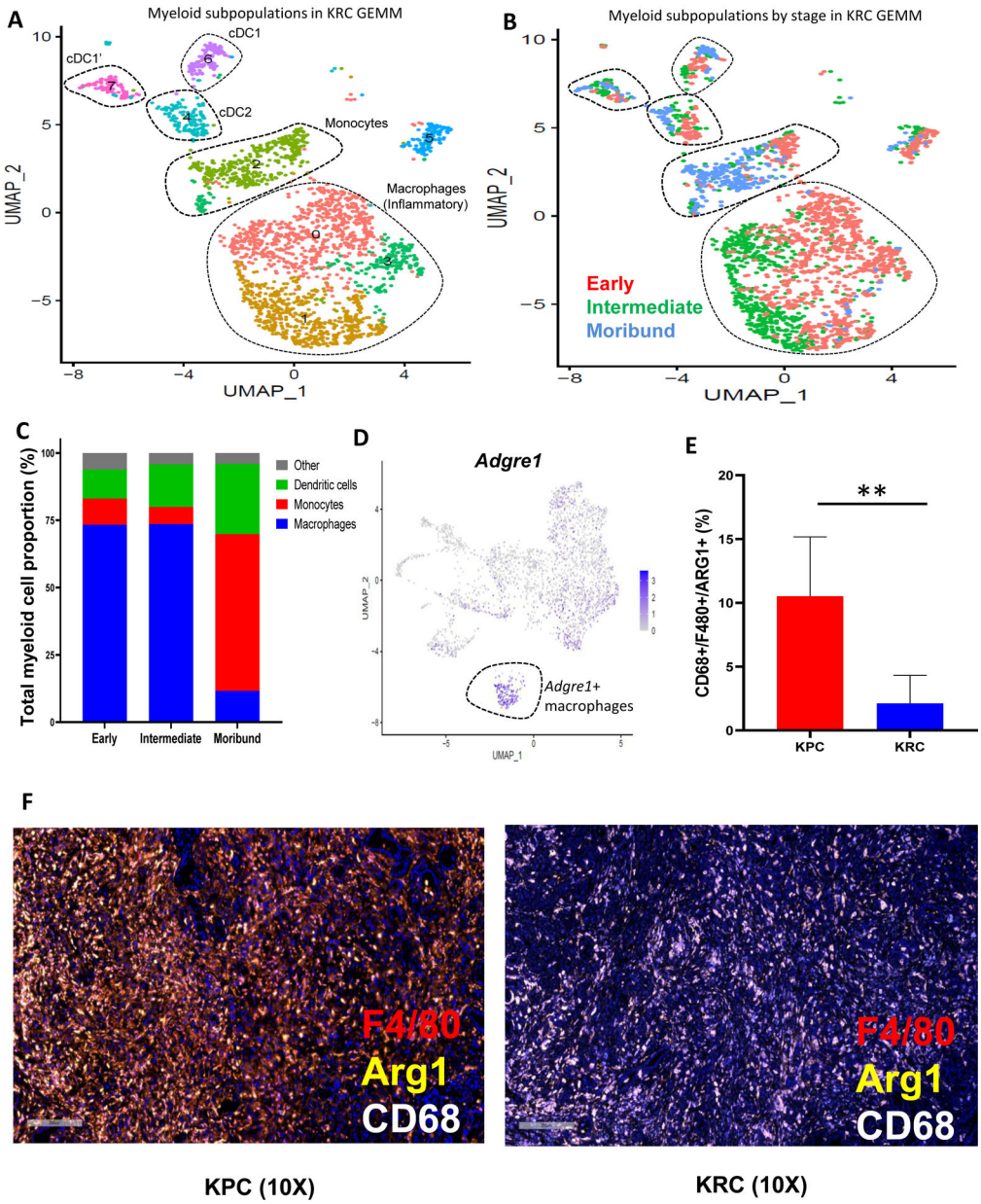

Figure 3: Myeloid focused scRNAseq analysis of the KRC GEMM.

(A) UMAP displaying all cells of myeloid lineage observed across the three KRC stages (early, intermediate, moribund) with a graph-based population delineation method applied to illustrate myeloid subpopulations. (B) Myeloid UMAP with each cell color coded according to KRC stage (early = red, intermediate = green, moribund = blue). (C) Summary bar graph denoting the percentage of each myeloid cell type observed in each of the three KRC stages analyzed. (D) Single gene UMAP of all myeloid cells in KPC and KRC GEMMs with *Adgre1* expression denoted. The tissue resident macrophage population is outlined. (E) Quantification of CD68, ARG1 and F4/80 immunofluorescence in KRC (n=4 tumors) and KPC (n=3 tumors) tissue sections. The percentage of cells positive for all three markers were averaged and displayed (two-sided t-test, *p<0.05). (F) Three color immunofluorescence

analysis of macrophage markers, CD68 (white), ARG1 (gold), F4/80 (red) and DAPI (blue), in KPC (left) and KRC (right) tumors. White scale bar: 200 μm.

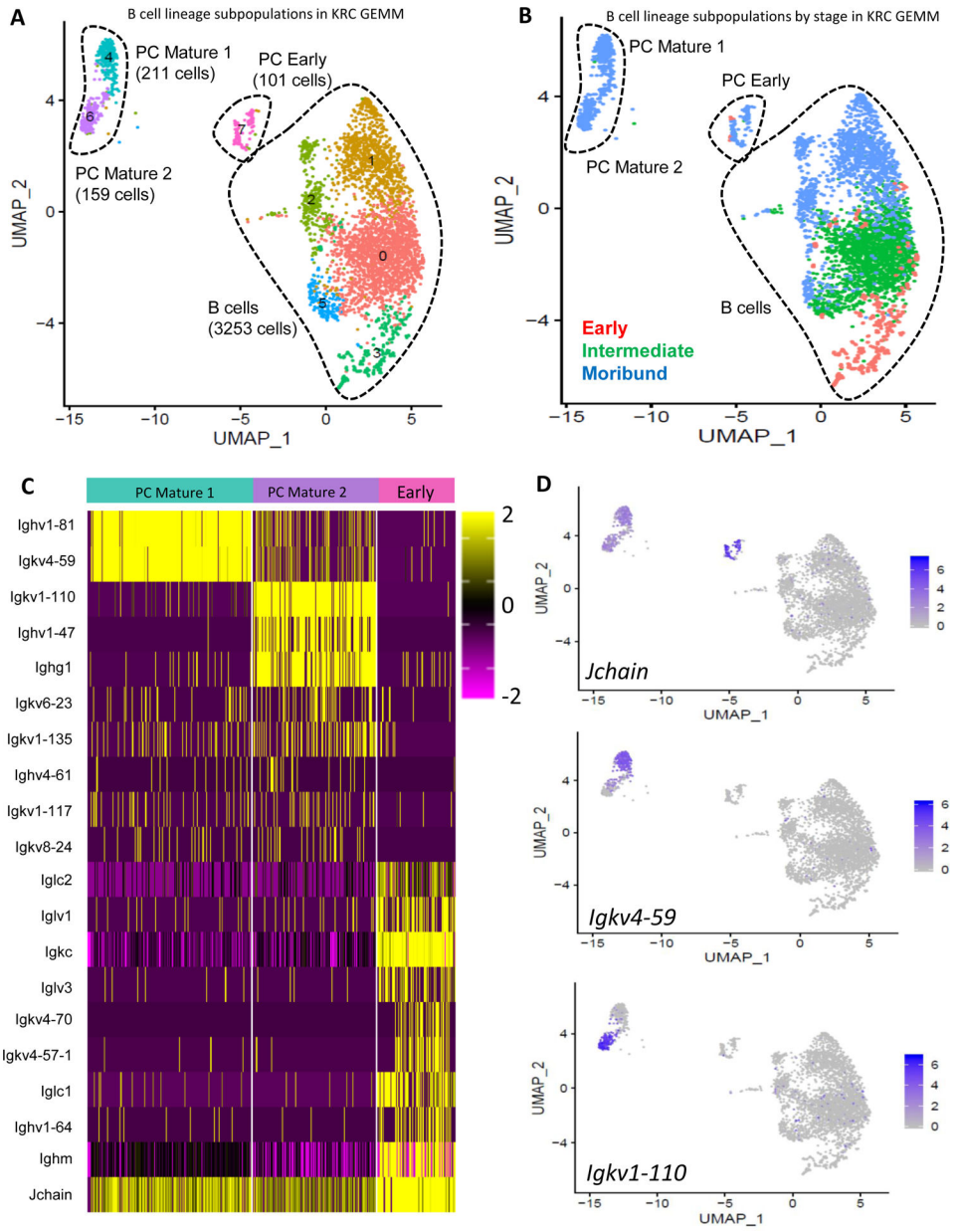

Figure 4: B cell lineage focused scRNAseq analysis of the KRC GEMM.

(A) UMAP displaying all cells of B cell lineage observed across the three KRC stages (early, intermediate, moribund) with a graph-based population delineation method applied to illustrate B lineage subpopulations. (B) B lineage UMAP with each cell color coded according to KRC stage (early = red, intermediate = green, moribund = blue). (C) Immunoglobulin (Ig) focused heatmap displaying Ig gene expression across the two mature and one early plasma cell subpopulations. Log color scale is noted to top-right of heatmap. (D) Single gene UMAP displaying specific markers for the early plasma cells (top; *Jchain*), mature plasma cell 1 (middle; *Igkv4-59*), and mature plasma cell 2 (bottom; *Igkv1-110*).

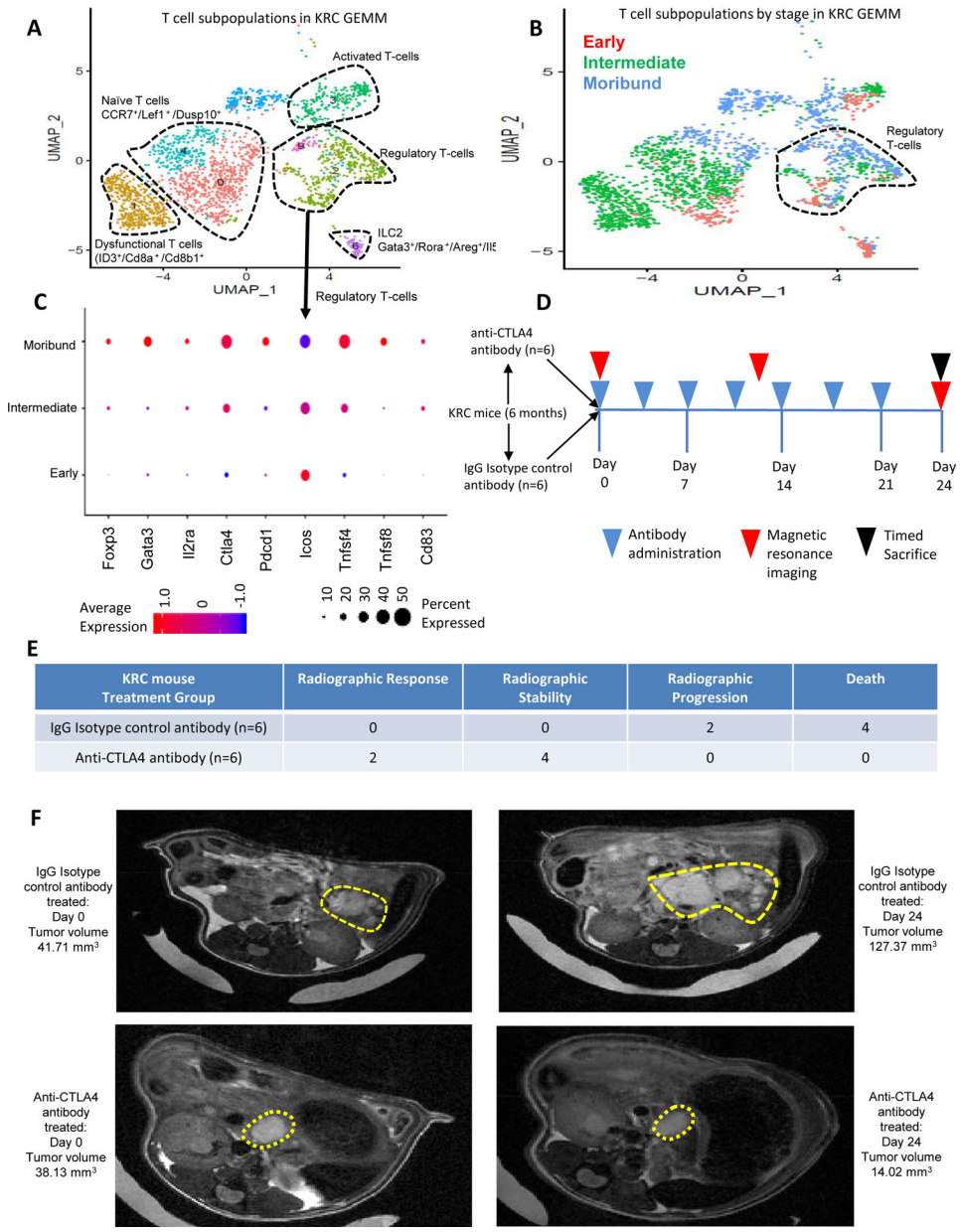

KRC mouse Treatment Group	Radiographic Response	Radiographic Stability	Radiographic Progression	Death
IgG Isotype control antibody (n=6)	0	0	2	4
Anti-CTLA4 antibody (n=6)	2	4	0	0

Figure 5: T-cell lineage focused scRNAseq analysis of the KRC GEMM.

(A) UMAP displaying all cells of T-cell lineage observed across the three KRC stages (early, intermediate, moribund) with a graph-based population delineation method applied to illustrate T lineage subpopulations. (B) T lineage UMAP with each cell color coded according to KRC stage (early = red, intermediate = green, moribund = blue). (C) Focused dot plot analysis displaying expression intensity and frequency of immune checkpoint genes in the regulatory T cell subpopulation. (D) Trial timeline schematic of KRC mice treated with either IgG isotype control antibody (n=6) or anti-CTLA4 antibody (n=6). Timing of antibody administration, MR imaging and planned animal sacrifice are all noted on the timeline. (E) Table displaying the results of the isotype control vs CTLA4 antibody treatment in KRC mice. (F) Representative axial T2 weighted MR images of longitudinally

followed KRC mice treated with isotype control antibody (top row) or anti-CTLA4 antibody (bottom row).

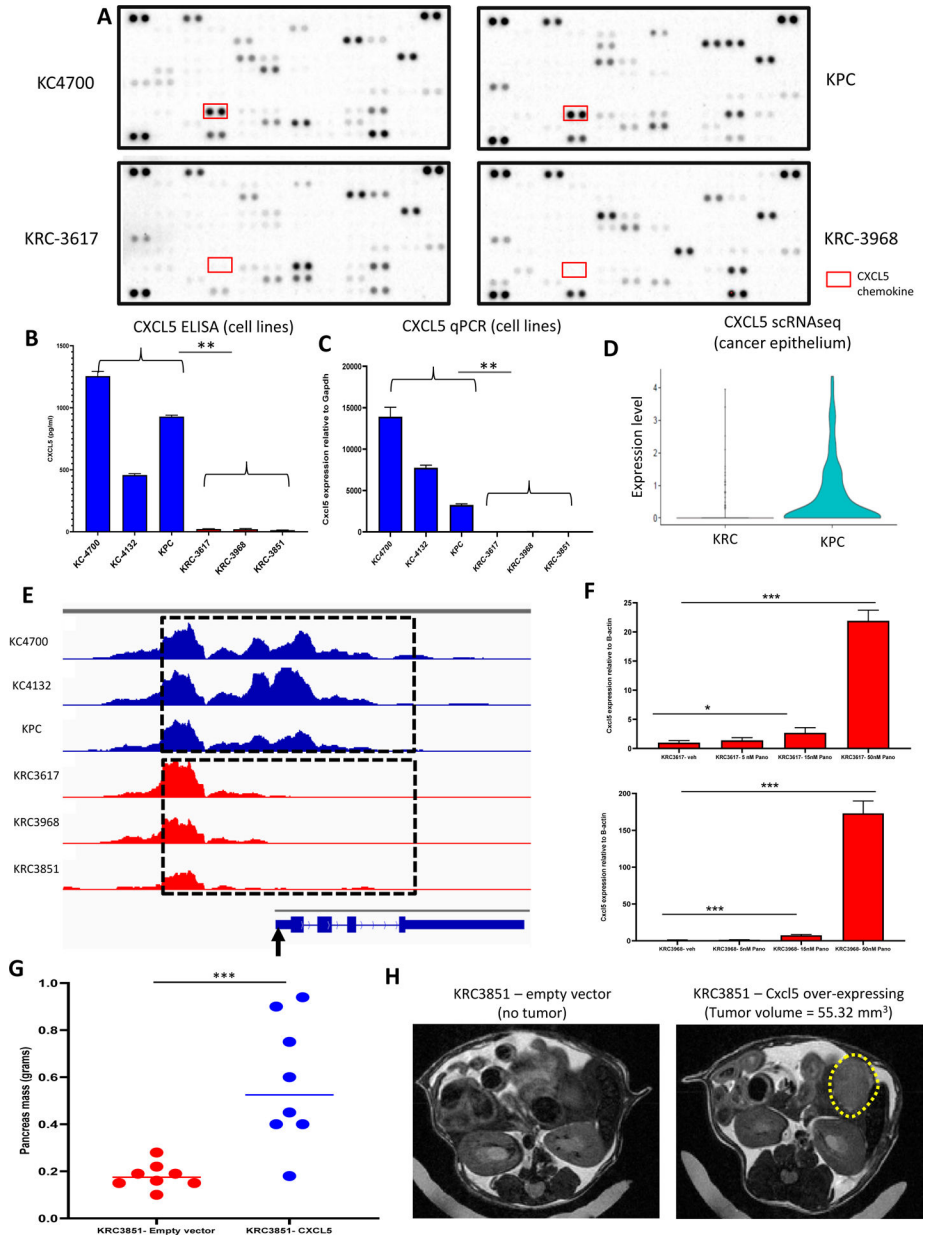

Figure 6: CXCL5 is downregulated in the KRC cancer epithelium.

(A) Mouse cytokine arrays displaying relative intensities of proteins secreted into the media after 48 hour incubation with KC (top, left) and KPC (top, right) cell lines or KRC cell lines (bottom). The red rectangle outlines the dots corresponding to CXCL5. (B) ELISA confirmation of mouse CXCL5 on 48-hour conditioned media from 3 *Rnf43* wild type and 3 KRC mouse PDAC cell lines. ** p<0.001, two-sided t-test comparing KRC vs *Rnf43* intact cell lines (C) Quantitative PCR analysis of *Cxcl5* in the same 3 *Rnf43* wild type and 3 KRC mouse PDAC cell lines. ** p<0.001, two-sided t-test comparing KRC vs *Rnf43* intact cell lines (D) Violin plot of *Cxcl5* expression scRNAseq datasets for KRC and KPC GEMMs. (E) ATAC-seq analysis of the transcription start site of *Cxcl5* in the 3 *Rnf43* wild type mouse PDAC cell lines and 3 KRC mouse PDAC cell lines. −3.47 log2 fold change (p=

5.52×10^{-7}) between the *Rnf43* wild type and KRC mouse PDAC cell lines (regions outlined by the hashed boxes). Vertical arrow indicates transcription start site. (F) qPCR analysis of *Cxcl5* in 2 KRC mouse PDAC cell lines treated with increasing doses of Panobinostat with all experiments done in triplicate (* $p<0.05$, ***$p<0.001$, one way ANOVA with Tukey's multiple comparison post-hoc test). (G) Pancreas masses at 4 weeks in mice orthotopically injected with a KRC cell line transduced with empty vector (red) or *Cxcl5* (blue). 10^5 cells/mouse were implanted in all experiments. The empty vector group (n = 8) had an average pancreas mass of 0.18g and the *Cxcl5* transduced group (n = 8) had an average tumor mass of 0.58g (***$p<0.001$, two-sided Student's t-test). (H) Representative T2 weighted MRI (axial view) of mice orthotopically implanted with empty vector transduced KRC cells (left) and *Cxcl5* transduced KRC cells (right).